11-2021

Uncertainty Analysis for CCD-augmented CASI® BRDF Measurement System

Todd V. Small
Air Force Institute of Technology

Samuel D. Butler
Air Force Institute of Technology

Michael A. Marciniak
Air Force Institute of Technology

Recommended Citation

Todd V. Small, Samuel D. Butler, and Michael A. Marciniak "Uncertainty analysis for CCD-augmented CASI® BRDF measurement system," Optical Engineering 60(11), 114101 (1 November 2021). https://doi.org/10.1117/1.OE.60.11.114101

Uncertainty analysis for CCD-augmented CASI® BRDF measurement system

Todd V. Small,* **Samuel D. Butler, and Michael A. Marciniak**
Air Force Institute of Technology, Department of Engineering Physics,
Wright-Patterson Air Force Base, Ohio, United States

Abstract. This work presents a measurement uncertainty analysis for a system designed to simultaneously capture specular in-plane and out-of-plane bidirectional reflectance distribution function (BRDF) data with high spatial resolution by augmenting the Complete Angle Scatter Instrument (CASI®) with a charge-coupled device (CCD) camera. Various scatter flux, incident flux, scatter angle, and detector solid angle uncertainty contributions are considered and evaluated based on imperfectly known system parameters. In particular, incident flux temporal fluctuation, detector noise and non-linearity, and out-of-plane aperture misalignment considerations each require significant adjustment from original CASI® uncertainty analysis, and expressions for neutral density (ND) filter, scatter angle, and solid angle uncertainties each require new formulations. Ultimately, ND filter uncertainty produces the largest contribution for the augmented system—at least when using unrefined worst-case tolerances—followed by solid angle uncertainty and pixel non-linearity. Total BRDF uncertainty and its contributing terms are compiled for several measurement scenarios, and compared with those from original analyses for single-pixel detectors. In particular, when ND filter uncertainty can be ignored or mitigated, total BRDF uncertainty values are comparable to those for the original system. [DOI: 10.1117/1.OE.60.11.114101]

Keywords: BRDF; optical scatter; reflectance; material surfaces; out-of-plane; remote sensing.

Paper 20210598 received Jun. 7, 2021; accepted for publication Oct. 12, 2021; published online Nov. 1, 2021.

1 Introduction

The bi-directional reflectance distribution function (BRDF) defines the spatial distribution of light reflected from a material surface as the ratio of scattered radiance to incident irradiance.[1] This ratio can be written purely in terms of measurable quantities as

$$f_r(\hat{\boldsymbol{\omega}}_i,\hat{\boldsymbol{\omega}}_s)=\frac{\delta\Phi_s}{\delta\Phi_i\cos\theta_s\delta\Omega_d}, \tag{1}$$

which is a particularly useful formulation for computing BRDF values from measurement data.[2,3] In this expression, $\hat{\boldsymbol{\omega}}_i$ and $\hat{\boldsymbol{\omega}}_s$ represent the incident and scattered directions, respectively, which are often written in spherical coordinates (θ_i,ϕ_i) and (θ_s,ϕ_s). The quantity $\delta\Phi_i$ is the total incident flux on a small material surface area; $\delta\Phi_s$ is the scattered flux measured by a small detector area, which subtends the solid angle $\delta\Omega_d$; and θ_s is the zenith angle between the material surface normal and the scattered direction.[4] For now, a single wavelength λ will be assumed, although f_r, $\delta\Phi_s$, and $\delta\Phi_i$ can all depend on wavelength as well. The δ symbols (denoting smallness of detector and sample illumination spot sizes) will be dropped for the rest of this work for clarity.

The Complete Angle Scatter Instrument (CASI®) excels at measuring absolute material BRDFs with high angular resolution within the plane of incidence (in-plane).[5] The CASI® traditionally employs single-pixel detectors to measure the scattered flux in one scatter direction dictated by detector arm location.[5] Augmenting the CASI® with a charge-coupled device (CCD) pixel array provides the ability to simultaneously measure scatter directions outside the

---

*Address all correspondence to Todd V. Small, todd.small@afit.edu plane of incidence (out-of-plane) with high spatial resolution, particularly surrounding specular peaks.[4,6]

The original uncertainty analysis for the CASI®[3] was built upon identifying uncertainties in various system parameters, and then quantifying how changes from nominal parameter values affect the overall BRDF calculation in Eq. (1). To remain conservative, the impacts of each system uncertainty on each variable were treated independently as first-order linear contributions and then added in quadrature.[3] The total BRDF relative uncertainty was first written as

$$\frac{\Delta f_r}{f_r} = \left[\left(\frac{\Delta\Phi_s}{\Phi_s}\right)^2 + \left(\frac{\Delta\Phi_i}{\Phi_i}\right)^2 + \left(\frac{\Delta\Omega_d}{\Omega_d}\right)^2 + \left(\frac{\Delta\theta_s \sin\theta_s}{\cos\theta_s}\right)^2\right]^{1/2}, \tag{2}$$

where the Δ symbols are used to denote changes from nominal. Each term in Eq. (2) was further subdivided in quadrature whenever multiple system uncertainties apply.

To conduct an uncertainty analysis for the CCD-augmented CASI®, each of the original uncertainties are examined and new uncertainties are considered. The uncertainty analysis presented in this paper ultimately builds upon original CASI® analysis methods[3] but also incorporates the fundamental differences of using a multi-pixel array detector.[4,6] Descriptions and definitions associated with the CCD-augmented CASI® system (including setup, alignment, coordinate systems, etc.) are carried forward from previous work.[4,6] This analysis will focus on CCD measurements centered on the specular peak, leaving considerations associated with off-specular measurements for future work. Polarizing elements are not incorporated, so polarization misalignment terms are ignored.

2 Uncertainty Linearization

Approximating an uncertainty as a first-order linear term can be useful, especially when the formulation can be written analytically. For example, the solid angle relative uncertainty for a circular aperture is derived by starting with the expression

$$\Omega_d = \frac{\pi r^2}{R^2}, \tag{3}$$

and then linearizing with respect to changes in each variable r and R, which becomes

$$\frac{\Delta\Omega_d}{\Omega_d} \approx \left[\left(\frac{\frac{\partial\Omega_d}{\partial r}\Delta r}{\Omega_d}\right)^2 + \left(\frac{\frac{\partial\Omega_d}{R}\Delta R}{\Omega_d}\right)^2\right]^{1/2} = \left[\left(\frac{2\Delta r}{r}\right)^2 + \left(\frac{2\Delta R}{R}\right)^2\right]^{1/2}. \tag{4}$$

In this case, computing and writing the partial derivatives is straightforward for each term.

However, when the expressions become more complicated, each term can also be calculated by evaluating the original expression itself, rather than using partial derivatives. For example, the solid angle relative uncertainty could also be written

$$\frac{\Delta\Omega_d}{\Omega_d} = \left[\left(\frac{\Omega_d|_{r+\Delta r,R} - \Omega_d|_{r,R}}{\Omega_d|_{r,R}}\right)^2 + \left(\frac{\Omega_d|_{r+,R+\Delta R} - \Omega_d|_{r,R}}{\Omega_d|_{r,R}}\right)\right]^{1/2}. \tag{5}$$

The latter technique will be implemented occasionally in this work for complex expressions.

3 Scatter Flux Uncertainty

This section addresses uncertainty in the scatter flux measurement Φ_s for each CCD pixel. Aside from polarization misalignment, the original analysis identified three sources of scatter flux uncertainty.[3] Out-of-plane aperture misalignment will be neglected while system noise and detector non-linearity contributions contain significant updates.

3.1 *Out-of-Plane Aperture Misalignment*

The original CASI® apertures translate in the out-of-plane direction (along the y axis) to align the measured scatter direction within the plane of incidence (usually by centering on the specular peak). However, accuracy limitations in the aperture movements and centering routines lead to scatter direction misalignment in the out-of-plane direction, where the scattered flux measurement differs from an ideal measurement located exactly in-plane.[3,5] Ultimately, with a single-pixel detector, the scattered flux lost due to this misalignment cannot be directly recovered, and the associated loss must be modeled as an uncertainty.

This term is not necessary for the CCD-augmented system, however, simply because it incorporates multi-pixel and microlens arrays. After following CCD alignment procedures,[4] the CCD still captures in-plane scattered flux within the pixel array, even with small misalignment. In other words, even when imperfectly centered on a specular peak, that peak is still clearly within the CCD frame. The in-plane flux simply shifts to other pixels in the array, rather than being clipped by the aperture.

Although out-of-plane (and other translational) misalignment impacts scatter direction in the CCD-augmented system, it no longer impacts scattered flux, so this term is no longer necessary.

3.2 *System Noise*

As stated in the original analysis, system noise contributes to scatter flux uncertainty through the noise-to-signal ratio.[3] Rather than calculating this term directly, though, detector noise limits can be characterized and then simply used to identify and ignore measurement regions near the noise level.[3,7] The same methodology will be employed in this section with extensions to the CCD-augmented system.

3.2.1 *Background reduction*

In its current configuration, the CCD lacks access to several background reduction features designed to help the original detectors operate near their inherent noise limits.

For instance, the CCD is not integrated with the chopper wheel and lock-in amplifiers used by the original detectors to suppress contributions from ambient light sources in the room.[5] Since the CCD is sensitive across the visible spectrum, room lights must be turned off or minimized to reduce background signal, especially as exposure time increases.

Also, no additional lens is placed in front of the CCD. The original detectors use a lens that constrains the field of view onto the material sample, thus reducing susceptibility to other background signals in the room, such as diffuse laser reflection from imperfect mirrors on the optical table. Lenses work for single-pixel detectors on the CASI® because they only measure flux in one scatter direction at a time. If a lens was placed in front of the CCD, each pixel would have an independent field of view, meaning each pixel would instead measure the flux reflected from a different location on the material sample, essentially imaging the material instead of measuring its BRDF. The lack of a lens allows each pixel in a single frame to measure the flux reflected into a unique scatter direction from a common illumination spot. However, without a lens, the pixel fields of view are constrained only by the camera aperture. When possible, physically blocking the camera's view of the laser path assists in reducing background interference.

Additionally, the original CASI® software automatically updates exposure time and detector gain and does not require the use of neutral density (ND) filters with typical low-power visible laser sources, even when measuring the beam signature directly. In contrast, CCD exposure time and gain values must be set manually, and in the absence of known laser damage thresholds, ND filters are required even with relatively low-power visible lasers, both to protect the pixel array and provide unsaturated specular measurements.[4]

The background signal for a system configuration can be characterized by taking flux readings with the laser on but blocked at the CASI® optics box output (prior to reaching the sample stage). In addition, inherent signal-independent detector noise characteristics (which excludes photon shot noise) can be characterized by taking flux readings with an aperture cover or lens cap on. When background flux readings approach detector noise flux readings, the system is operating near the detector noise limit.

3.2.2 *Minimum and maximum BRDF measurements*

Ultimately, when limited by detector noise rather than background contributions, the noise equivalent BRDF is directly proportional to the detector's noise equivalent flux, but varies inversely with incident flux and detector solid angle.[7] Using a 15-mW helium–neon (HeNe) laser at 632.8 nm wavelength, the noise floor of the original CASI® using a silicon-based detector was validated through measurement at $\sim 5 \times 10^{-8}\ \mathrm{sr}^{-1}$.[5,7]

Conversely, for an ideal specular material, represented by the beam signature, the CASI® detector aperture can collect nearly the entire beam's flux within a single solid angle at the specular peak. In this case, the ratio of scattered flux to incident flux approaches unity, and the maximum measurable BRDF approaches $1/\Omega_d$. Using its smallest aperture, the maximum BRDF value of the original CASI® system is $\sim 3.5 \times 10^{6}\ \mathrm{sr}^{-1}$.[7] Thus, the original system is capable of measurements spanning nearly 15 orders of magnitude.

In the CCD-augmented system, measurements are typically captured using 1, 10, 100, and 1000 ms exposure times with default gain and black level offsets.[4] With an individual pixel saturation limit of 16,383 digital counts (DC), the results from each exposure time are scaled and stitched together,[4] so scattered flux values for each pixel can range from zero to $\Phi_{s,\mathrm{high}} = 1.6383 \times 10^{7}$ scaled digital counts (sDC). Although longer exposure times are possible with this camera, in practice, the benefit wanes beyond 1000 ms due to background signal and time-dependent detector noise contributions.

With the CCD, incident flux is calculated by summing all pixel outputs from a stitched beam signature after subtracting the background.[4] To remain just below the pixel saturation limit with an unimpeded 15-mW red HeNe laser, the beam must be attenuated by ND filters with a total optical density (OD) of 5.2.[4] With 5.2 OD and a maximum exposure time of 1000 ms, a representative incident flux summation yields 9.828×10^{9} sDC.

In the BRDF calculation, the ratio Φ_s/Φ_i matters, not the absolute values of each.[3] When incident flux is calculated from the beam signature with ND filters in place, that incident flux value remains valid for any scattered flux measurements using the exact same ND filters. However, when scattered flux measurements are made with less OD than the beam signature, then the ratio Φ_s/Φ_i must be compensated. This can be accomplished by adjusting Φ_i according to

$$\Phi_i = \Phi_b \times 10^{(\mathrm{OD}_b - \mathrm{OD}_m)}, \tag{6}$$

where Φ_b represents the incident flux summation using the ND filter attenuation OD_b for the beam signature, OD_m indicates the ND filter attenuation used for the scattered flux measurement, and Φ_i now becomes the incident flux adjusted for the difference in ND filters. As should be expected, when $\mathrm{OD}_m = \mathrm{OD}_b$, then $\Phi_i = \Phi_b$, with no incident flux adjustment required.

Using the 15-mW red HeNe laser source, background measurements were captured after reducing background interference as much as practical. After scaling and stitching, the mean pixel output across the entire array was 48.05 sDC with a standard deviation of 23.11 sDC. For comparison, when the lens cap was installed, the mean pixel output was only slightly lower at 45.88 sDC with a similar standard deviation, demonstrating that the CCD-augmented system was operating near the detector noise limit (within 5%). The scatter flux lower limit can thus be expressed $\Phi_{s,\mathrm{low}} = 48.05$ sDC. Due to their location in the optics box, the ND filters attenuate the signal with negligible changes to the background, so $\Phi_{s,\mathrm{low}}$ does not change with OD_m.

The noise equivalent BRDF and its associated standard deviation for the CCD-augmented system using the 15-mW red HeNe laser can then be calculated by substituting Eq. (6) into Eq. (1), and then also substituting the nominal values $\cos\theta_s = 1$, $\Omega_d = 2.864 \times 10^{-10}\ \mathrm{sr}^{-1}$,[4,6] $\Phi_b = 9.828 \times 10^{9}$ sDC, and $\mathrm{OD}_b = 5.2$. Then, the scattered flux Φ_s is set first to the lower operating limit $\Phi_{s,\mathrm{low}}$ and then to its standard deviation. When $\mathrm{OD}_m = \mathrm{OD}_b$, when measuring an ideal or highly reflective surface, the noise equivalent BRDF is $17.07\ \mathrm{sr}^{-1}$ with a standard deviation of $8.21\ \mathrm{sr}^{-1}$. If however $\mathrm{OD}_b - \mathrm{OD}_m = 1.1$,[6] such as the case when measuring a polished aluminum sample,[6] the noise equivalent BRDF and standard deviation reduce to $1.36\ \mathrm{sr}^{-1}$

and 0.65 sr^{-1}, respectively. Finally, if scattered flux measurements are made without ND filters so that $\mathrm{OD}_m = 0$, then the minimum measurable BRDF reaches $1.08 \times 10^{-4}\ \mathrm{sr}^{-1}$, with a standard deviation of $5.18 \times 10^{-5}\ \mathrm{sr}^{-1}$.

If the source beam could be focused onto a single pixel with the appropriate OD_b to stay below pixel saturation, then $\Phi_s = \Phi_i$ in Eq. (1), and the maximum measurable BRDF when $\mathrm{OD}_m = \mathrm{OD}_b$ theoretically becomes $1/\Omega_d = 3.5 \times 10^9\ \mathrm{sr}^{-1}$. In practice though, the red HeNe laser focuses to a minimum $1/e^2$ width of ∼25 pixel widths. Instead, the practical peak BRDF value can be calculated by substituting $\Phi_{s,\mathrm{high}}$ into Eq. (1). When $\mathrm{OD}_m = \mathrm{OD}_b$, for ideal or highly reflective measurements, the maximum measurable BRDF value becomes $5.82 \times 10^6\ \mathrm{sr}^{-1}$. When $\mathrm{OD}_b - \mathrm{OD}_m = 1.1$, as in the polished aluminum measurements, the maximum measurable BRDF becomes $4.62 \times 10^5\ \mathrm{sr}^{-1}$. Finally, if $\mathrm{OD}_m = 0$, the maximum BRDF decreases to 36.7 sr^{-1}.

3.2.3 *Dynamic range*

Ultimately, for any stitched measurement composed of exposure times from 1 to 1000 ms with a fixed OD_m, as is the case for measurements centered on the specular peak, the CCD-augmented system can measure BRDF values spanning approximately $\log_{10}(\Phi_{s,\mathrm{high}}/\Phi_{s,\mathrm{low}}) = 5.53$ orders of magnitude. For the sake of comparison, the ideal noise-free dynamic range would span $\log_{10}(\Phi_{s,\mathrm{high}}) = 7.21$ orders of magnitude. If OD_m is increased or decreased, depending on the magnitude of the material's specular peak, the maximum and minimum measurable BRDF values shift accordingly, but still span 5.53 orders of magnitude within a single stitched CCD frame, representing a bit more than one-third of the original CASI's® dynamic range.

In theory, by rotating the CASI® detector arm to shift the CCD away from the specular direction, it becomes possible to safely reduce OD_m from $\mathrm{OD}_m = \mathrm{OD}_b$, perhaps all the way to $\mathrm{OD}_m = 0$. The maximum achievable dynamic range could then increase to $\log_{10}(\Phi_{s,\mathrm{high}}/\Phi_{s,\mathrm{low}}) + \mathrm{OD}_b$. For the 15-mW red HeNe laser source where $\mathrm{OD}_b = 5.2$, the maximum theoretical dynamic range would become 10.7 orders of magnitude, or two-thirds of the original CASI's® dynamic range. However, this extension requires investigating impacts when the specular peak is shifted off the pixel array, such as stray reflections inside the camera aperture.

3.3 *Non-Linearity*

In the original CASI® uncertainty analysis, detector linearity was evaluated by adding an ND filter to attenuate the source beam, and then comparing the expected and actual change in detector response.[8] The resulting error was limited to a maximum of 1% with software correction.[3] In the CCD-augmented system, though, each pixel functions as an independent detector, and each requires its own linearity evaluation, which cannot be readily accomplished by attenuating a highly focused Gaussian source laser. Specifications for our particular CCD list a maximum signal error due to non-linearity differences (1%), but this value is only valid from 10% to 90% saturation.[9] Furthermore, this linearity reporting may be in terms of average pixel response,[10] rather than the linearity of each pixel individually.

Following standard camera characterization methods,[10] the CCD was centered 32 in from the 4 in aperture of an Electro-Optical Industries ISV410 integrating sphere with no lens or lens tube. Measurements were taken under continuously adjustable uniform illumination as 66-frame averages (limited by maximum individual file size) with 1 ms exposure. Ten luminance values – 50, 100, 300, 500, 1000, 1500, 2000, 2500, 3000, and 3200 foot-Lamberts (ft-L) – were selected ranging from the sphere's minimum achievable stable luminance to near-saturation. At 50 ft-L, the average pixel reading was 292 DC (1.78% saturation), with a maximum of 336 DC and a minimum of 256 DC (1.56% saturation), all above the noise floor. At 3200 ft-L, the average pixel reading was 15,155 DC (92.5% saturation), with a minimum of 12,994 DC and a maximum of 15,636 DC (95.4% saturation), all below saturation.

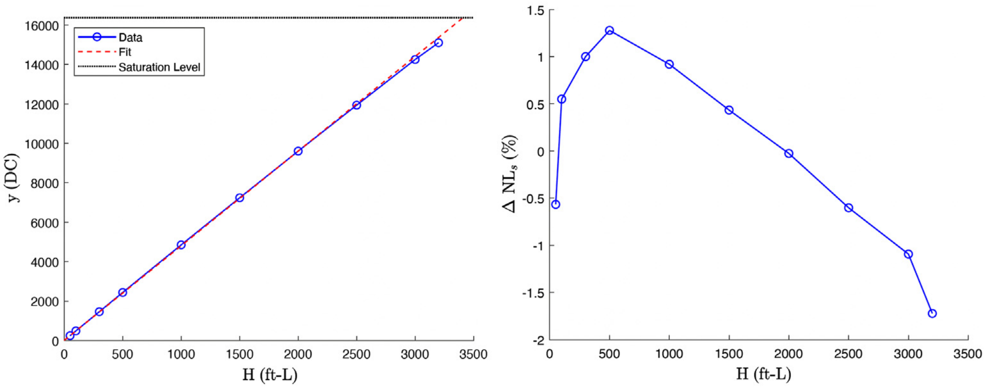

(a) (b)

Fig. 1 Nonlinearity evaluation for the array-wide average pixel response. Both the measured array-wide average pixel response and its linear regression are plotted in (a) in terms of digital counts (up to the pixel saturation limit) as functions of illumination. The relative difference between the measured average response and its regression is plotted in (b), showing the maximum nonlinearity value of 1.72% located at the highest luminance level of 3200 ft-L.

As a baseline for comparison, CCD linearity was first computed using only the range of luminance values that induced 10% to 90% saturation (500 to 3000 ft-L), fitting a single linear regression to the array-wide pixel averages for each luminance. Using a standard formulation, the linearity errors at each luminance level were calculated as the relative difference between the measured array-wide pixel averages and the regression,[10] expressed as

$$\Delta \mathrm{NL}_s[i] = \frac{y[i] - (a_0 + a_1 H[i])}{(a_0 + a_1 H[i])}. \tag{7}$$

In Eq. (7), $H[i]$ represents the indexed set of scalar luminance values, $y[i]$ is the indexed set of scalar array-wide pixel averages measured at each luminance, and a_0 and a_1 are scalar linear regression fit parameters.[10] The linearity error $\Delta \mathrm{NL}_s[i]$ is then a scalar value at each luminance. The resulting maximum linearity error was 0.64%. When the regression parameters and linearity errors were re-calculated using the full luminance range (50-3200 ft-L), the maximum linearity error increased to 1.72%. Figure 1(a) plots both the measured array-wide average pixel response and its linear regression (up to the pixel saturation limit) as functions of luminance level, and Fig. 1(b) shows the linearity error reaching its maximum absolute value at 3200 ft-L. Unfortunately, though, this baseline method compresses the linearity characterization to a single value for the entire array at each luminance level.

Two additional methods extended the baseline method in order to isolate and characterize individual pixel linearity. In the first method, linear regression parameters were generated for each individual pixel's response over the full luminance range, and then linearity errors were calculated as the relative difference between each individual measured pixel response and its own regression at each luminance. Thus, in Eq. (7), $y[i]$ became an array of individual pixel measurements at each luminance, a_0 and a_1 became arrays comprised of regression fit parameters for each pixel, and the linearity error $\Delta \mathrm{NL}_s[i]$ became an array comprised of error values for each pixel at each luminance. $\Delta \mathrm{NL}_s[i]$ could then be condensed by finding the maximum error for each pixel across all luminance values. Using this method, the maximum linearity error among all pixels was 3.52%, whereas the average linearity error for each pixel was 1.74% with a standard deviation of 0.14%. Although this method evaluates the linearity of each pixel independently, it does not capture differences in each pixel's response relative to a common baseline.

The final method combines the others and defines linearity error as the relative difference between each individual pixel response and the array-wide linear regression, ultimately describing each pixel's individual photo-response relative to a common array-wide average linear response. In this method, $y[i]$ remains the array of individual pixel measurements at each luminance, but a_0 and a_1 remain the scalar regression fit parameters from the array-wide pixel averages. Here, $\Delta\mathrm{NL}_s[i]$ is still an array comprised of error values for each pixel at each luminance but now referenced to a single common regression. Again, $\Delta\mathrm{NL}_s[i]$ can be condensed by finding the maximum error for each pixel across all luminance values. Using this method, the maximum linearity error among all pixels was 16.32%, whereas the average linearity error for each pixel was 2.18% with a standard deviation of 0.50%.

The final method will be used to assign a maximum non-linear error value $\Delta\mathrm{NL}_s$ to each pixel independently, taking into account non-uniformities among pixel photo-responses. Although the overall maximum error is rather high at over 16%, such values are significant outliers, and could either be corrected or ignored as desired. For example, for this particular CCD, only 0.021% of pixels exceed an error of 5.19%, or six standard deviations above the average error.

3.4 *Combined Scatter Flux Uncertainty*

In summary, aperture misalignment is not applicable, and although system noise is characterized, it is left to visual identification. Thus, the only contributing term for scatter flux relative uncertainty becomes pixel non-linearity

$$\frac{\Delta\Phi_s}{\Phi_s} = [\Delta\mathrm{NL}_s^2]^{1/2}, \tag{8}$$

where $\Delta\mathrm{NL}_s$ is an array containing the maximum non-linear error for each pixel relative to the array-wide average linear response. Since $\Delta\mathrm{NL}_s$ can be negative, the root mean square yields a positive value.

4 Incident Flux Uncertainty

This section addresses uncertainty in measured incident flux Φ_i. Aside from polarization misalignment, the original analysis identified four sources of scatter flux uncertainty.[3] The detector noise and aperture area effects remain negligible but non-linearity and temporal contributions are adjusted. An extra term is incorporated to address ND filter uncertainty.

4.1 *System Noise*

As described in the original CASI® analysis, the same noise-to-signal ratio affects the detector output whether measuring incident or scatter flux, and so the noise contribution was not directly included within the incident flux uncertainty calculation.[3] Even though the CCD measures incident flux by summing over the entire array of pixels, this term can still be omitted. By averaging the beam signature over a maximum number of frames (66) and subtracting the detector-limited background measurement, noise contributions can be neglected.

4.2 *Non-Linearity*

For the original single-pixel CASI® detectors, the same linearity error derived as part of the scatter flux uncertainty was also included as part of the incident uncertainty.[3] With a CCD, non-linear responses still affect each pixel when measuring the beam signature, but since the pixel outputs are summed, the average non-linear response matters more. At the focused 15-mW red HeNe minimum spot size, the $1/e^2$ beam width, which includes ∼86% of the beam's power, still encompasses more than 1850 pixels. When linearity error terms are calculated using the final method from Sec. 3.3, the average pixel non-linearity across the entire array and dynamic range is

$$\Delta\mathrm{NL}_i = 0.018\%. \tag{9}$$

This single scalar value becomes the non-linearity contribution $\Delta\mathrm{NL}_i$ to incident flux uncertainty.

4.3 *Aperture Area*

Even when measuring incident flux from a focused Gaussian beam using the largest available aperture, part of the signal inevitably falls outside the collection area. The original CASI® detectors have circular apertures, but our particular CCD has a rectangular array with square pixels.[4] The relative flux outside the rectangular array can be approximated as

$$\frac{\Delta\Phi_A}{\Phi_A} = 1 - \operatorname{erf}\left(\frac{\sqrt{2}a}{w}\right)\operatorname{erf}\left(\frac{\sqrt{2}b}{w}\right), \tag{10}$$

where a and b represent the pixel indices at the edge of the array, and w is the $1/e^2$ radius of the focused laser spot on the CCD. For an array with 3296×2472 square pixels, a becomes 1648 and b becomes 1236. A numerical value for w can be found by performing a non-linear least squares fit to the 15-mW red HeNe laser's Gaussian beam signature, yielding ∼25 pixel widths. When these values are substituted into Eq (10), the expression evaluates to zero within machine precision:

$$\left.\frac{\Delta\Phi_A}{\Phi_A}\right|_{w=25} \approx 0. \tag{11}$$

Thus, the aperture area term can be neglected for the CCD-augmented system.

4.4 *Temporal Fluctuations*

The original CASI® detectors utilize a reference detector to monitor source power and correct for short-term fluctuations during scatter measurements, which allows for neglecting temporal uncertainty contributions.[3] However, the CCD is not integrated with a reference detector.

To evaluate the stability of the 15-mW red HeNe laser source, a NIST-calibrated photodiode power meter collected more than 1.5 h of power readings at 16.6 frames per second (fps).[4] Due to individual file size limitations, the data was collected in roughly 15 min sets. The first collection began immediately after turning on the laser, with immediate transitions into the second and third sets. The fourth collection began the next day, again immediately after turning on the laser, with immediate transitions into the fifth and sixth sets.

At most, due to individual file size limitations, our particular CCD collects 66 full frames at 2.3 fps, which spans ∼28.7 s. Each set of power meter data can be converted into rolling 28.7 s averages, representing possible windows in which the CCD incident flux measurement occurs. The relative difference can be found between each rolling average and the overall 15 min average for the set, and this process can be repeated for each set. In both cases, as expected, the maximum relative difference was much higher within the first 15 min, before the laser had a chance to sufficiently stabilize. However, after the first 15 min, the maximum relative difference in incident flux within a 15 min measurement window was 0.72%.

The same process can be repeated when the CCD collects smaller numbers of frames for a beam signature. For instance, when the CCD collects only five full frames at 2.3 fps, each incident flux collection spans ∼2.17 s, and the power meter data is instead converted into 2.17 s rolling averages. Once again, the maximum difference relative to the overall 15 min average was much higher within the first 15 min but afterward peaked at 1.01%.

Rather than neglecting temporal flux relative uncertainty, it will be set to a single scalar value

$$\frac{\Delta\Phi_T}{\Phi_T} = 1.01\%, \tag{12}$$

which contributes to each pixel uniformly.

4.5 *Optical Density Uncertainty*

As shown in Eq. (6), the measurement and scaling of Φ_i depends on the difference between OD_b and OD_m. In practice, the best OD for remaining just below saturation can require stacking multiple ND filters so that OD_b can be written $\mathrm{OD}_{b1} + \mathrm{OD}_{b2} + \dots + \mathrm{OD}_{bn}$, and OD_m can be written $\mathrm{OD}_{m1} + \mathrm{OD}_{m2} + \dots + \mathrm{OD}_{mk}$, where n and k indicate the total number of filters in each combination. For example, the 5.2 OD required for beam signature measurement can be accomplished by stacking $\mathrm{OD}_{b1} = 4.0$, $\mathrm{OD}_{b2} = 1.0$, and $\mathrm{OD}_{b3} = 0.2$. Likewise, the 4.1 OD necessary for measuring a polished aluminum sample can be accomplished by stacking $\mathrm{OD}_{m1} = 4.0$ and $\mathrm{OD}_{m2} = 0.1$.

The set of absorptive ND filters available for this work have published OD tolerances based primarily on uncertainty in filter thickness during production. Unfortunately, from a transmission percentage standpoint, the published tolerances are rather large at higher OD values. For example, for a wavelength of 632.8 nm, the 0.1, 0.2, and 0.3 OD filters have a tolerance of ±0.01 OD, which corresponds to transmission uncertainties of 2.33% each, while the 4.0 OD filter has a tolerance of ±0.2 OD, which alone corresponds to a transmission uncertainty of 58.5%.

The relative uncertainty in incident flux due to uncertainties in OD can be written by linearizing Eq. (6) with respect to changes in each OD value

$$\frac{\Delta\Phi_{\mathrm{OD}}}{\Phi_{\mathrm{OD}}} = \ln(10)\sqrt{\Delta\mathrm{OD}_{b1}^2 + \dots + \Delta\mathrm{OD}_{bn}^2 + \Delta\mathrm{OD}_{m1}^2 + \dots + \Delta\mathrm{OD}_{mk}^2}. \tag{13}$$

If certain ND filters are repeated in both OD_b and OD_m, those terms can be omitted, because despite any tolerance, the actual value for an individual filter is constant.

It is important to note that this OD uncertainty depends largely on the ND filters required to measure a specific material, and ND filter transmission tolerances may vary with wavelength. However, any OD uncertainty values represent a constant contribution across all pixels. Baseline published uncertainties represent worst-case knowledge, which could be significantly improved with independent wavelength-specific filter characterization. For combined relative uncertainty calculations in Sec. 7, results will be presented using both worst-case and perfect OD uncertainties for comparison.

4.6 *Combined Incident Flux Uncertainty*

In summary, system noise and aperture area considerations can be ignored for incident flux relative uncertainty. The relevant contributions become pixel non-linearity, temporal fluctuation, and ND filter uncertainties, which can be combined as

$$\frac{\Delta\Phi_i}{\Phi_i} = \left[\Delta\mathrm{NL}_i^2 + \left(\frac{\Delta\Phi_T}{\Phi_T}\right)^2 + \left(\frac{\Delta\Phi_{\mathrm{OD}}}{\Phi_{\mathrm{OD}}}\right)^2\right]^{1/2}. \tag{14}$$

Each term represents a single scalar value, which is uniformly valid for every pixel measurement within a single stitched CCD frame.

5 Scatter Angle Uncertainty

This section addresses uncertainty in the scatter angles associated with each pixel during a CCD measurement. In the original analysis for single-pixel detectors making in-plane measurements, uncertainty in θ_s depends only on the uncertainty in the material sample's normal direction and the angular precision of the detector arm;[3,11] uncertainty in ϕ_s was not relevant. During a CCD measurement, though, each pixel maps to a unique (θ_s, ϕ_s) combination, which depends on pixel index (n_h, n_v), pixel dimensions d_h and d_v, the distance R from material sample to CCD location, and detector arm offset angle θ_c.[6] This section describes how uncertainties in each parameter except for pixel index affect θ_s and ϕ_s even with perfect CCD alignment, and then describes a formulation for characterizing how CCD alignment uncertainty can further affect the scatter angles. Uncertainty in pixel index is assumed to be negligible for the scientific-grade CCD camera, however, by assuming the microlens array eliminates photon spillover between adjacent pixels.

5.1 *Uncertainty with Perfect Alignment*

The equations for θ_s and ϕ_s assuming perfect alignment are provided in previous work.[6] Our current CCD has square pixels so that $d_h = d_v = d$.

5.1.1 *Uncertainty in θ_s*

By using partial derivatives, the relative uncertainty in θ_s due to the uncertainty ΔR is

$$\frac{\Delta\theta_{s_R}\,\sin\theta_s}{\cos\theta_s} = \left(\frac{R}{d^2(n_h^2 + n_v^2) + R^2} + \frac{1}{dn_h \tan\theta_c - R}\right)\Delta R, \tag{15}$$

where the scaling factor $\sin\theta_s/\cos\theta_s$ comes from Eq. (2). The relative contribution from $\Delta\theta_{s_R}$ is always zero at the center pixel where $(n_h, n_v) = (0{,}0)$, which makes intuitive geometric sense. Moving the CCD closer to or farther from the material sample would not change the scatter direction for the center pixel.

Similarly, the relative uncertainty in θ_s due to the uncertainty Δd can be written as

$$\frac{\Delta\theta_{s_d}\,\sin\theta_s}{\cos\theta_s} = \left(\frac{d(n_h^2 + n_v^2)}{d^2(n_h^2 + n_v^2) + R^2} + \frac{n_h}{R\cot\theta_c - dn_h}\right)\Delta d. \tag{16}$$

The relative contribution from $\Delta\theta_{s_d}$ is also always zero at the center pixel where $(n_h, n_v) = (0{,}0)$, which again makes intuitive geometric sense, because changing pixel size does not alter the scatter direction of the center pixel.

Lastly, the relative uncertainty in θ_s due to the uncertainty $\Delta\theta_c$ can be written as

$$\frac{\Delta\theta_{s_c}\,\sin\theta_s}{\cos\theta_s} = \left(\frac{dn_h\cos\theta_c + R\sin\theta_c}{R\cos\theta_c - dn_h\sin\theta_c}\right)\Delta\theta_c. \tag{17}$$

Notably, this uncertainty contribution does not depend at all on vertical pixel index n_v, meaning changes in detector arm location affect changes in θ_s equivalently for pixels in the same column.

5.1.2 *Uncertainty in ϕ_s*

Although ϕ_s does not appear directly in the BRDF calculation given by Eq. (1), this angle is important for annotating each pixel's scatter coordinates for data analysis. The equation for ϕ_s assuming perfect alignment is also provided in previous work.[6]

By using partial derivatives, the relative uncertainty in ϕ_s due to the uncertainty ΔR is

$$\frac{\Delta\phi_{s_R}}{\phi_s} = -\frac{dn_v\sin\theta_c}{d^2n_v^2 + (dn_h\cos\theta_c + R\sin\theta_c)^2}\frac{\Delta R}{\phi_s}. \tag{18}$$

Notably, this relative uncertainty is zero if either $n_v = 0$ or $\theta_c = 0$, which makes intuitive sense. When the horizontal pixel row is aligned perfectly in-plane, changing the CCD's distance from the material sample does not change the azimuthal plane for those pixels. In addition, when the center of the CCD is lined up directly with the material surface normal, changing the distance does not change the azimuthal plane for any pixel, even though the zenith angles θ_s change.

Similarly, the relative uncertainty in ϕ_s due to the uncertainty Δd can be written as

$$\frac{\Delta\phi_{s_d}}{\phi_s} = \frac{n_vR\sin\theta_c}{d^2n_v^2 + (dn_h\cos\theta_c + R\sin\theta_c)^2}\frac{\Delta d}{\phi_s}. \tag{19}$$

This relative uncertainty also equals zero if either $n_v = 0$ or $\theta_c = 0$, which again makes intuitive geometric sense. When the horizontal pixel row is perfectly aligned in-plane, changing the pixel size does not change the azimuthal plane for the center pixel row. In addition, when the center of the CCD is lined up directly with the material surface normal, changing the pixel size does not change the azimuthal plane for any pixel, despite changing the zenith angles θ_s.

Finally, the relative uncertainty in ϕ_s due to the uncertainty $\Delta\theta_c$ can be written

$$\frac{\Delta\phi_{s_c}}{\phi_s} = \frac{dn_v(dn_h \sin\theta_c - R\cos\theta_c)}{d^2n_v^2 + (dn_h\cos\theta_c + R\sin\theta_c)^2}\frac{\Delta\theta_c}{\phi_s}. \tag{20}$$

This relative uncertainty is zero if $n_v = 0$, which means that when perfectly aligned, changing the detector arm angle does not change the azimuthal plane for the center horizontal row of pixels.

In each of Eqs. (18)–(20), a mathematical discontinuity exists when n_h, n_v, and θ_c all equal zero simultaneously. However, the discontinuities each resolve when the appropriate limits are taken.

5.1.3 *Numeric values*

The uncertainty ΔR arises from imperfect knowledge of the distance between the CCD and material sample. Combining use of a tape measure and camera specifications,[4] ΔR rounds up conservatively to 5 mm. The uncertainty Δd arises from imperfect knowledge of pixel size. When Δd exceeds 4×10^{-9} m, the size of the full array would no longer round to any of its listed dimensions, so this value serves as a conservative upper bound. Finally, the uncertainty $\Delta\theta_c$ arises from imperfect knowledge of the absolute angle between the material surface normal and the CCD's position as controlled by rotating the detector arm. For most specular materials, physics dictates that $\theta_s = \theta_i$ at the center of the specular peak, so similar to the original system, θ_c is most easily determined by rotating the detector arm to center the CCD on the specular peak, and then assuming that $\theta_c = \theta_i$. Uncertainty in θ_c can then be traced to uncertainty in θ_i, as well as rotation stage accuracy tolerances. Conservatively, $\Delta\theta_c$ can be estimated at 0.5 deg.[11]

When these numeric values for ΔR, Δd, and $\Delta\theta_c$ are substituted into Eqs. (15)–(20), the resulting relative uncertainties in θ_s and ϕ_s vary from pixel to pixel. For example, Table 1 compiles the maximum scatter angle uncertainty contributions within the pixel array for several θ_c measurement geometries with perfect alignment.

5.2 *Uncertainty from Imperfect Alignment*

Even after following an iterative process to align the CCD with a specular peak,[4] the CCD is likely to possess some combination of rotational and translational misalignment. The uncertainty in each scatter angle due to misalignment will be labeled $\Delta\theta_{s_m}$ and $\Delta\phi_{s_m}$.

Table 1 Array-wide maximum relative scatter angle uncertainty contributions for three different θ_c measurement geometries. In reality, scatter angle uncertainties vary from pixel to pixel, but array-wide maximum values provide a conservative metric. Values here assume perfect CCD alignment, and are given in percentage (%).

Array-Wide Max Values	$\theta_c = 20$ deg (%)	$\theta_c = 40$ deg (%)	$\theta_c = 60$ deg (%)
$\frac{\Delta\theta_{s_R}\sin\theta_s}{\cos\theta_s}$	0.018	0.039	0.080
$\frac{\Delta\theta_{s_d}\sin\theta_s}{\cos\theta_s}$	8.34×10^{-4}	0.0018	0.038
$\frac{\Delta\theta_{s_c}\sin\theta_s}{\cos\theta_s}$	0.35	0.77	1.61
$\frac{\Delta\phi_{s_R}}{\phi_s}$	0.036	0.017	0.012
$\frac{\Delta\phi_{s_d}}{\phi_s}$	0.0017	8.13×10^{-4}	5.81×10^{-4}
$\frac{\Delta\phi_{s_c}}{\phi_s}$	0.056	0.012	0.0042

5.2.1 *Misalignment formulation*

The CCD's orientation can be described as a rotation applied to the perfectly aligned and projected pixel vectors, defined in previous work as $\vec{r}_p$ relative to the (x, y, z) coordinate axes.[6] Any generic orientation can be expressed as a chained series of three Euler rotations, as long as the axis of the second rotation is orthogonal to both the axes of the first and third rotations[12] but for now the general rotation will be designated simply as $\mathbb{R}_{\mathrm{CCD}}$.

Apart from rotational misalignment, the center of the CCD may also be slightly offset from the actual center of the specular peak. In-plane alignment is actuated by detector arm rotation, but out-of-plane alignment is actuated by a vertical linear translation stage.[4] At the measurement location, the CCD still carries the orientation defined by $\mathbb{R}_{\mathrm{CCD}}$, which in theory affects the apparent location of pixel offset manifestations. However, for small residual angles following iterative alignment, this particular effect will be ignored. As a result, the Cartesian scatter vectors for each pixel from previous work[6] can be rewritten to include misalignment

$$\vec{r}_s = \mathbb{R}_y(\theta_c + \Delta\theta_{c_m})(\mathbb{R}_{\mathrm{CCD}}\vec{r}_p + R\hat{z}) + \Delta y\hat{\mathbf{y}}. \tag{21}$$

Here, $\Delta\theta_{c_m}$ and Δy represent the in-plane angular offset and out-of-plane translational offset, respectively. If m_h and m_v are the apparent in-plane and out-of-plane pixel offsets from the center of the specular peak, then $\Delta\theta_{c_m} = m_h(9.70\text{ deg} \times 10^{-4})$ and $\Delta y = m_v(5.50\ \mu\text{m})$, where $9.70\text{ deg} \times 10^{-4}$ is the linear angle subtended by each pixel near the CCD center and 5.50 μm is the pixel width.[4] The scatter angles θ_s and ϕ_s for each pixel are then computed using the previously defined spherical coordinate conversion.[6]

To implement a specific rotation within Eq. (21), the general rotation $\mathbb{R}_{\mathrm{CCD}}$ is replaced with the Tait-Bryan rotation series $\mathbb{R}_z(\theta_r)\mathbb{R}_y(\theta_y)\mathbb{R}_x(\theta_p)$. The roll, yaw, and pitch misalignment angles θ_r, θ_y, and θ_p can be directly measured and approximated during the CCD alignment process.[4] Although different rotation series could also sufficiently represent the CCD orientation, this particular order best matches the measurement setup. When alignment procedure motions are modeled by extending Eq. (21), this particular choice allows the change in horizontal pixel index to mathematically reach zero when $\theta_y = 0$, and allows the change in vertical pixel index to mathematically reach zero when either $\theta_r = 0$ or $\theta_p = 0$.

5.2.2 *Numeric values*

In previous work, a single example alignment iteration resulted in $\theta_r = 0.11$ deg, $\theta_y = 0.062$ deg, and $\theta_p = 0.025$ deg;[4] these angles remain valid for any subsequent measurements without CCD orientation readjustment. Values for m_h and m_v, however, vary independently for every specific measurement. Perhaps the simplest quantitative way to determine m_h and m_v is to compare the location of the peak pixel reading to the center of the pixel array.

The absolute uncertainties $\Delta\theta_{s_m}$ and $\Delta\phi_{s_m}$ are then computed as the difference between the nominal values for θ_s and ϕ_s assuming perfect alignment[6] and the values including misalignment. Relative differences require the scaling used in Eqs. (15)–(20).

For example, in a previously published broadband metallic mirror measurement when $\theta_i = 20$ deg,[6] the peak pixel reading shows $m_h = 3$ and $m_v = 5$. The resulting relative misalignment uncertainties in θ_s and ϕ_s vary with pixel, but the maximum values in this case are 0.0034% and 0.012%, respectively. As another example, in a polished aluminum measurement when $\theta_i = 40$ deg,[6] peak pixel readings show $m_h = -1$ and $m_v = -1$, with maximum relative uncertainties of 0.0049% and 0.0036%, respectively. Finally, for a Kapton® measurement when $\theta_i = 60$ deg, the peak pixel reading shows $m_h = 72$ and $m_v = -3$, with maximum relative uncertainties of 0.23% and 0.0045%, respectively.

5.3 *Combined Scatter Angle Uncertainty*

In summary, pixel scatter angle uncertainty depends on uncertainty in the distance between material sample and CCD, uncertainty in the angle between detector arm and material surface normal, uncertainty in pixel width, and CCD rotational and translational misalignment. The relative uncertainties can be combined in quadrature as

$$\frac{\Delta\theta_s \sin \theta_s}{\cos \theta_s} = \frac{\sin \theta_s}{\cos \theta_s} [\Delta\theta_{s_r}^2 + \Delta\theta_{s_d}^2 + \Delta\theta_{s_c}^2 + \Delta\theta_{s_m}^2]^{1/2}, \tag{22a}$$

$$\frac{\Delta\phi_s}{\phi_s} = \frac{1}{\phi_s} [\Delta\phi_{s_R}^2 + \Delta\phi_{s_d}^2 + \Delta\phi_{s_c}^2 + \Delta\phi_{s_m}^2]^{1/2}. \tag{22b}$$

Each term represents an array of values for each individual pixel within a stitched measurement.

6 Solid Angle Uncertainty

This section addresses relative uncertainty in the solid angle Ω_d subtended by each pixel during a CCD measurement. As with the original detectors, this uncertainty still depends on uncertainty in pixel dimensions and the distance R, but now accounts for an array of square pixels. Uncertainties are first described assuming perfect alignment, and then a formulation is presented for characterizing how uncertainty in CCD alignment can also impact the solid angles.

6.1 *Uncertainty with Perfect Alignment*

The equation for Ω_d assuming perfect alignment is provided in previous work.[6] As in Sec. 5, pixel dimensions are assumed equal so that $d_h = d_v = d$.

By using partial derivatives, the relative uncertainty in Ω_d due to the uncertainty ΔR is

$$\frac{\Delta\Omega_{d_R}}{\Omega_d} = \left(\frac{1}{R} - \frac{3R}{d^2(n_h^2 + n_v^2) + R^2}\right)\Delta R, \tag{23}$$

which has a minimum at the center pixel. Similarly, the uncertainty in Ω_d due to the uncertainty Δd can be written

$$\frac{\Delta\Omega_{d_d}}{\Omega_d} = \left(\frac{2R^2 - d^2(n_h^2 + n_v^2)}{dR^2 + d^3(n_h^2 + n_v^2)}\right)\Delta d, \tag{24}$$

which has a maximum at the center pixel.

6.2 *Uncertainty from Imperfect Alignment*

CCD rotational and translational misalignment can also contribute to solid angle uncertainty. Although the solid angle of each pixel does not depend on θ_c, it does depend on θ_d, defined as the angle between the pixel normal direction and the pixel scatter vector $\vec{r}_s$.[6] The solid angle with misalignment can be computed

$$\Omega_d \approx \frac{d^2 \cos \theta_d}{|\vec{r}_s|^2} = \frac{d^2(\vec{r}_s|_{\theta_c=0} \cdot \mathbb{R}_{\mathrm{CCD}}\hat{z})}{|\vec{r}_s|_{\theta_c=0}|^3}, \tag{25}$$

where the vector $\vec{r}_s$ is evaluated using Eq. (21) with $\theta_c = 0$. The rotational misalignment $\mathbb{R}_{\mathrm{CCD}}$ can still be incorporated as the Tait–Bryan rotation from Sec. 5.2.1, but the translational misalignment offsets m_h and m_v are instead derived from the beam signature. With perfect alignment at $\theta_c = 0$, the pixel normal directions would each match the $\hat{z}$ direction.

The absolute uncertainties $\Delta\Omega_{d_m}$ and $\Delta\Omega_{d_m}$ are then computed as the difference between the nominal values for Ω_d assuming perfect alignment[6] and the values including misalignment. Dividing by the nominal values for Ω_d gives the relative uncertainty.

6.3 *Numeric Values*

Using the same values for ΔR and Δd from Sec. 5.1.3, the maximum relative uncertainty in Ω_d due to the uncertainty ΔR is 3.08%, whereas the maximum relative uncertainty in Ω_d due to the uncertainty Δd is 0.15%. Then, using the same rotational misalignment angles from Sec. 5.2.2, and beam signature translational misalignment offset $m_x = -1$ and $m_y = -1$, the largest relative uncertainty in Ω_d due to misalignment is 0.012%.

6.4 *Combined Solid Angle Uncertainty*

In summary, pixel solid angle uncertainties depend on uncertainties in the distance between material sample and CCD, pixel width, and CCD rotational and translational misalignment. The relative uncertainties can be combined in quadrature as

$$\frac{\Delta\Omega_d}{\Omega_d} = \frac{1}{\Omega_d}[\Delta\Omega_{d_R}^2 + \Delta\Omega_{d_d}^2 + \Delta\Omega_{d_m}^2]^{1/2}. \tag{26}$$

Each term represents an array of values for each individual pixel within a stitched frame.

7 Total Uncertainty

The total relative measurement uncertainty can now be calculated by substituting the combined scatter flux, incident flux, scatter angle, and solid angle relative uncertainty terms into Eq. (2). The results are applied to CCD measurement data and compared to original CASI® uncertainty analysis.

7.1 *Array Average Uncertainties*

Table 2 compiles relative uncertainty statistics across the entire pixel array for two different specular peak measurements, demonstrating how the total uncertainty and each contribution change with both incident angle and ND filter uncertainty. The left half displays uncertainty results for normal incidence and $\mathrm{OD}_m = \mathrm{OD}_b$, when both θ_c and $\Delta\Phi_{\mathrm{OD}}/\Phi_{\mathrm{OD}}$ are zero. These conditions apply, for example, when converting beam signatures directly into BRDF values. The right half then demonstrates uncertainty results with $\theta_i = 60$ deg, $\mathrm{OD}_b = 5.2$, and $\mathrm{OD}_m = 3.5$, which corresponds to $\theta_c = 60$ deg and $\Delta\Phi_{\mathrm{OD}}/\Phi_{\mathrm{OD}} = 59.7\%$ with worst-case OD

Table 2 Total relative BRDF uncertainty and contributing terms for two specular CCD measurements, compiled as array-wide average, standard deviation, maximum, and minimum values, in percentage (%). The left half corresponds to normal incidence with $\mathrm{OD}_m = \mathrm{OD}_b$. The right half corresponds to $\theta_s = 60$ deg with $\mathrm{OD}_b = 5.2$ and $\mathrm{OD}_m = 3.5$. The bottom row demonstrates the impact of OD uncertainty mitigation.

	$\theta_i = 0$ deg				$\theta_i = 60$ deg			
	Avg (%)	Std Dev (%)	Max (%)	Min (%)	Avg (%)	Std Dev (%)	Max (%)	Min (%)
$\frac{\Delta f_r}{f_r}$	3.93	0.300	16.6	3.41	59.8	0.0211	61.9	59.8
$\frac{\Delta\Phi_s}{\Phi_s}$	2.18	0.502	16.3	1.05	2.18	0.502	16.3	1.05
$\frac{\Delta\Phi_i}{\Phi_i}$	1.01	0	1.01	1.01	59.7	0	59.7	59.7
$\frac{\Delta\theta_s \sin\theta_s}{\cos\theta_s}$	0.0122	0.00703	0.0244	0	1.53	0.0569	1.63	1.43
$\frac{\Delta\Omega_d}{\Omega_d}$	3.08	0.00122	3.08	3.07	3.08	0.00122	3.08	3.07
$\left.\frac{\Delta f_r}{f_r}\right\vert_{\frac{\Delta\Phi_{\mathrm{OD}}}{\Phi_{\mathrm{OD}}}=0}$	3.93	0.300	16.6	3.41	4.22	0.282	16.7	3.72

uncertainty. These conditions apply, for example, to Kapton® specular peak measurement data from previous work.[6] The bottom row compares total relative uncertainty between the cases when OD uncertainty is totally mitigated.

In general, Table 2 shows several key features. First, depending on the ND filters used, worst-case OD uncertainty can easily provide the largest source of uncertainty in the BRDF calculation. However, like the other incident flux uncertainties, this term is applied uniformly to every pixel, and so does not affect the relative shape of the BRDF across a single stitched frame. On average, solid angle uncertainty provides the second largest source of relative uncertainty. For the original CASI® detectors, the smallest aperture carried ∼2% relative uncertainty,[3] slightly <3% relative uncertainty for each CCD pixel. On average, pixel non-linearity provides the third largest source of relative uncertainty, just above 2%, although a small number of outliers possess up to 16%. Scatter angle relative uncertainty contributions increase with θ_s, as expected from the original analysis,[3] up to an average of ∼1.5% near 60 deg.

According to these numbers, the easiest way to reduce total relative uncertainty would be to mitigate OD uncertainty by independently characterizing each ND filter rather than relying on broad published production tolerances. In addition, differences in pixel linearity could be software corrected to an average response, and outlier pixels could be selectively ignored.

7.2 *Specific Pixel Uncertainties*

Finally, Table 3 displays total relative uncertainty results for several specific in-plane scatter angles as part of two additional specular peak CCD measurement cases. Here, $\theta_i = 20$ deg and 40 deg are chosen to match Butler's analysis using original CASI® measurements at these angles.[11] For the $\theta_i = 20$ deg case, $\text{OD}_b = 5.2$ and $\text{OD}_m = 5.0$ are chosen to mimic previous mirror CCD measurements,[6] where $\Delta\Phi_{\text{OD}}/\Phi_{\text{OD}} = 2.30\%$ in the worst-case. For the $\theta_i = 40$ deg case, $\text{OD}_b = 5.2$ and $\text{OD}_m = 4.1$ are chosen to mimic previous polished aluminum CCD measurements,[6] where $\Delta\Phi_{\text{OD}}/\Phi_{\text{OD}} = 14.2\%$ in the worst-case. The in-plane angles are written as deviations from specular ($\theta_s - \theta_i$) and then matched to appropriate pixels in the CCD's center horizontal row. For the sake of comparison, total relative uncertainty is also presented when OD uncertainty is completely mitigated.

In the original analysis, out-of-plane aperture misalignment comprised the largest portion of relative uncertainty nearest the specular peak–up to 12% out of 17% total uncertainty.[3,11] However, this contribution diminished monotonically away from the specular peak. Total uncertainties reduced to a minimum of 7.5% somewhere between $\theta_s - \theta_i = 0.5$ deg and 1 deg, before increasing again due to scatter angle relative uncertainty contributions.[3,11] The out-of-plane term no longer applies to the CCD, as described in Sec. 3.1, and as a result, the total uncertainty values

Table 3 Total relative BRDF uncertainty for two specular CCD measurements, reported from individual pixels corresponding to specific in-plane specular offset angles ($\theta_s - \theta_i$). Values are given as percentages (%), with separate columns including and omitting ND filter uncertainty. On the left half, $\theta_i = 20$ deg, $\text{OD}_b = 5.2$, and $\text{OD}_m = 5.0$. On the right half, $\theta_i = 40$ deg, $\text{OD}_b = 5.2$, and $\text{OD}_m = 4.1$.

	$\theta_i = 20$ deg		$\theta_i = 40$ deg	
$\theta_s - \theta_i$	$\frac{\Delta f_r}{f_r}\Big\rvert_{\frac{\Delta\Phi_{\text{OD}}}{\Phi_{\text{OD}}}=2.30\%}$ (%)	$\frac{\Delta f_r}{f_r}\Big\rvert_{\frac{\Delta\Phi_{\text{OD}}}{\Phi_{\text{OD}}}=0}$ (%)	$\frac{\Delta f_r}{f_r}\Big\rvert_{\frac{\Delta\Phi_{\text{OD}}}{\Phi_{\text{OD}}}=14.2\%}$ (%)	$\frac{\Delta f_r}{f_r}\Big\rvert_{\frac{\Delta\Phi_{\text{OD}}}{\Phi_{\text{OD}}}=0}$ (%)
0.011 deg	5.05	4.50	14.9	4.54
0.022 deg	4.45	3.81	14.7	3.86
0.05 deg	4.36	3.70	14.7	3.76
0.1 deg	4.38	3.73	14.7	3.79
0.5 deg	4.24	3.57	14.7	3.63
1.0 deg	4.83	4.24	14.8	4.30

no longer increase so dramatically approaching the specular peak. Instead, individual pixel non-linearity and OD uncertainty largely determine how CCD uncertainties compare to the original CASI®. When a pixel's non-linearity is near the array's average, and when OD uncertainty is low, then overall CCD uncertainty is similar or even less than the original CASI®.[3,11] When either non-linearity or OD uncertainty is relatively high, then the overall CCD uncertainty eclipses the original values.

7.3 *Comparison to Original CASI®*

Figure 2 offers a visualization by overlaying the total relative uncertainty bounds onto both an in-plane slice and an out-of-plane slice through the beam signature CCD measurement data. The in-plane slice extracts BRDF values from each pixel along the CCD's middle row, whereas the out-of-plane slice extracts BRDF values from each pixel along the CCD's middle column. The center of the CCD is aligned with the center of the beam, and so each pixel provides an independent BRDF measurement and maps to a particular angular offset from center, spanning the angular range displayed on the horizontal plot axis. When BRDF values are shown on a log scale over the full dynamic range, as in Fig. 2(a), the CCD uncertainty bounds are indistinguishable from the measurement data; there is no OD uncertainty for the beam signature and so the average total uncertainty remains below 4% (See Table 2). Figures 2(b) and 2(c) zoom in successively toward the center of the specular peak, where the uncertainty bounds are finally discernible in Fig. 2(c).

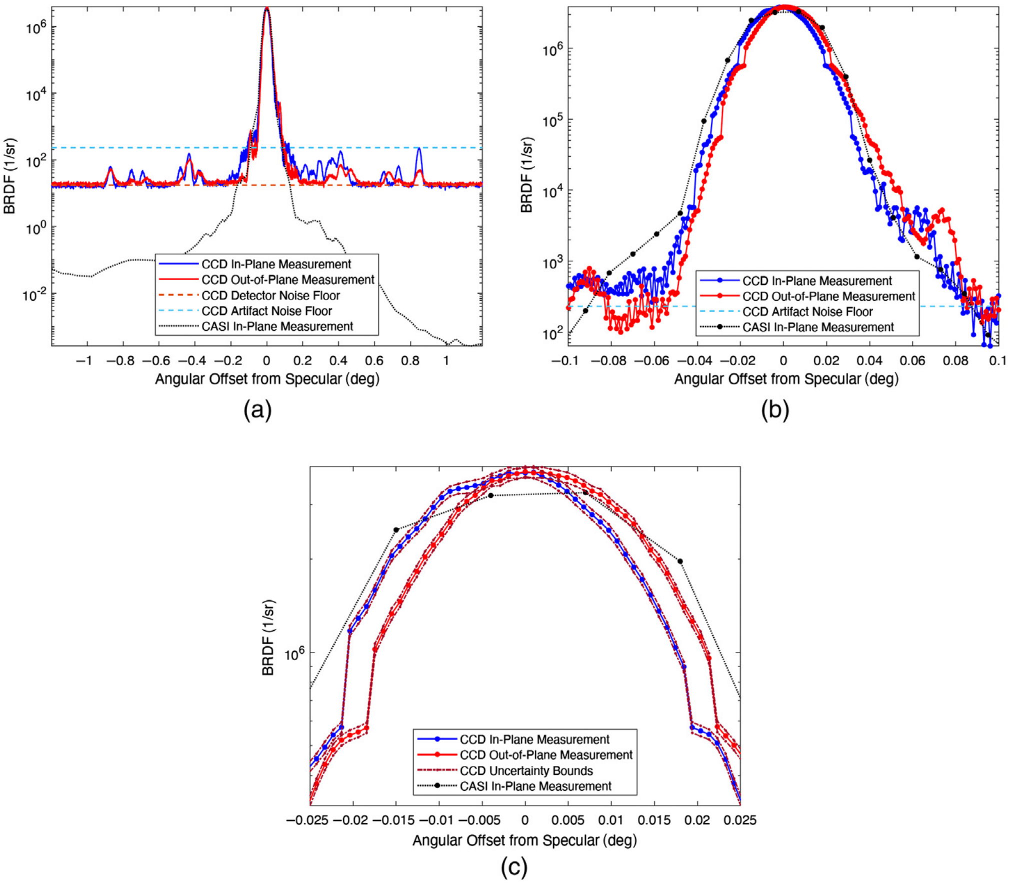

(a)

(b)

(c)

Fig. 2 Plots of beam signature measurement data using a 15-mW red HeNe laser source. CCD measurements were collected as one stitched frame using 1, 10, 100, and 1000 ms exposures with 5.2 OD. In-plane and out-of-plane pixel results, uncertainty bounds, and noise floors based on both inherent detector noise and measurement artifacts are shown. In-plane CASI® measurements using the appropriate original detector are shown in black. The full CCD angular extent is plotted in (a), with successive zoom near the specular peak in (b) and (c). Since the average total uncertainty remains below 4%, the CCD uncertainty bounds finally become visible in (c).

For comparison, beam signature measurement data from the original CASI® is also overlaid. It is important to note that due to the difference in the distance R, the beam must be refocused when switching between the CCD and original detector, so a perfect overlay is unrealistic. Nevertheless, given that the CASI® step size is 0.011 deg and the CCD pixel size is $9.70\ \text{deg} \times 10^{-4}$, there is quite good agreement near the specular peak, both in terms of maximum value, beam width, and beam shape.[4]

As expected, the CCD lacks the dynamic range of the original system, especially within a single stitched frame, but it does possess higher spatial resolution. In addition, the CCD detects two potentially undesirable features, which the original detectors do not. First, high-frequency diffractive noise is noticeable in Fig. 2(b). Second, the CCD registers several sub-peaks, which were first identified in previous work[4,6] and are now evident in Fig. 2(a). However, as shown in Fig. 2, the uncertainty bounds and detector noise analysis conducted in this work are not wide enough to explain or absorb either characteristic. In particular, when revisiting previous work describing and demonstrating the stitching process,[4] the sub-peaks are not visible until exposure time is sufficiently long, which further strengthens the argument that the sub-peaks represent physical stray light signals. Pending further investigation, these features may arise from stray light from this particular camera's protective IR blocking filter or the ND filters. For instance, the diffractive noise may be explained as scatter from particles on imperfectly clean filters, and the sub-peaks may arise from multiple reflections at the filter interfaces. Unlike the original detectors, the CCD does not incorporate a lens, and so even though stray light may exist within the original detector optics, the CCD allows stray signals to spatially register on different pixels.

Further investigation of these artifacts will be left to future work. In particular, measurements taken while successively slewing the CCD away from the center of the specular peak may provide further insight and mitigation of the sub-peaks. For now, though, data analysis can still be performed by filtering out such features. In particular, since the sub-peaks are still more than 4.8 orders of magnitude below the main peak, an adjusted artifact noise floor can easily be implemented, as shown in Fig. 2(a).

8 Conclusion

In summary, an uncertainty analysis was performed for the CCD-augmented CASI® BRDF measurement system. Cady's original uncertainty analysis[3] served as a blueprint and starting point but required significant updates and additions. Notably, the out-of-plane aperture misalignment term, which had previously served as the dominant uncertainty source for near-specular measurements, was no longer necessary as a source of scatter flux uncertainty. Detector nonlinearity and incident flux temporal fluctuation both demanded reassessment, scatter angle and solid angle relative uncertainty expressions each required new analytical derivations, and detector noise limits needed reevaluation. In addition, new terms were devised to account for OD uncertainty and CCD misalignment.

Ultimately, the largest uncertainty term was shown to be OD uncertainty in certain cases, although it varied from 0% to almost 60%, depending on the ND filters used for different measurements and their known tolerances. Solid angle uncertainty was the second largest contributor, with relative uncertainties slightly larger than those in the original analysis, consistently near 3%. On average, detector non-linearity was the third largest term, just above 2% relative uncertainty, although a very small number of outlier pixels possess up to 16%. Scatter angle uncertainty increases with θ_s up to ∼1.5% near $\theta_s = 60\ \text{deg}$.

The simplest way to reduce the total relative uncertainty, then, would be to independently characterize each ND filter and tighten the OD uncertainty. The method presented in Sec. 4.5 for calculating OD uncertainty remains generic for any wavelength, but the numeric ND filter tolerance values are most likely functions of wavelength, requiring wavelength-dependent characterization. However, when OD uncertainty is negligible, the typical total relative uncertainties for nearly any scatter angle are in the vicinity of 4%, compared to minimum uncertainties near 2% in Cady's analysis,[3] or 7.5% in Butler's analysis.[11]

Finally, the CCD sacrifices nearly two-thirds of the dynamic range of the original CASI® when making measurements centered on the specular peak, but gains almost ten times greater spatial resolution. Although beam signature CCD measurements agree well with equivalent CASI® in-plane data, the CCD encounters two potentially undesirable artifacts: (1) high-frequency diffractive noise, and (2) multiple sub-peaks. The uncertainty bounds and noise analysis from this work are not wide enough to explain or absorb either characteristic, but due to the relatively small impact from each, they can be filtered prior to further data analysis.

Acknowledgments

This material is based upon work supported by the Air Force Office of Scientific Research (AFOSR) under award number F4FGA09014J002. The authors declare no conflicts of interest.

Code, Data, and Materials Availability

Data underlying the results presented in this paper are not publicly available at this time but may be obtained from the authors upon reasonable request.

References

1. F. Nicodemus, “Directional reflectance and emissivity of an opaque surface,” Appl. Opt. **4**, 767–775 (1965).
2. J. Maxwell and J. Beard, *Bidirectional Reflectance Model Validation and Utilization*, Environmental Research Institute of Michigan (ERIM) Technical Report AFAL-TR-73-303 (1973).
3. F. Cady et al., “BRDF error analysis,” Proc. SPIE **1165**, 154–164 (1990).
4. T. Small, S. Butler, and M. Marciniak, “Augmenting CASI® BRDF measurement device to measure out-of-plane scatter with CCD pixel array,” Proc. SPIE **11485**, 114850B (2020).
5. J. Rifkin et al., “Design review of a complete angle scatter instrument,” Proc. SPIE **1036**, 116–124 (1989).
6. T. Small, S. Butler, and M. Marciniak, “Scatter coordinate mapping and out-of-plane BRDF measurements for specular materials using an augmented CASI® measurement system,” Proc. SPIE **11727**, 117270X (2021).
7. T. Schiff et al., “Maximum and minimum limitations imposed on BSDF measurements,” Proc. SPIE **0967**, 50–57 (1989).
8. F. Cady et al., “Linearity in BSDF measurements,” Proc. SPIE **1165**, 192–203 (1990).
9. ON Semiconductor®, “KAI-08051: 3296 (H) x 2472 (V) interline CCD image sensor,” (Rev 5.: Dec 2015), https://www.onsemi.com/pdf/datasheet/kai-08051-d.pdf (accessed 8 May 2020).
10. European Machine Vision Association, “EMVA Standard 1288: Standard for characterization of image sensors and cameras,” (Release 3.1: 30 Dec 2016), https://www.emva.org/wp-content/uploads/EMVA1288-3.1a.pdf (accessed 16 Dec. 2020).
11. S. Butler, S. Nauyoks, and M. Marciniak, “Experimental measurement and analysis of wavelength-dependent properties of the BRDF,” Proc. SPIE **9611**, 96110G (2015).
12. H. Goldstein, C. Poole, and J. Safko, *Classical Mechanics*, 3rd ed., Pearson Education Inc. (2002).

Todd V. Small is a major in the United States Air Force and an assistant professor at the Air Force Institute of Technology (AFIT). He received his BS and MS degrees in astronautical engineering from the United States Air Force Academy and the Massachusetts Institute of Technology, respectively, and recently completed his PhD from AFIT. His research interests include bidirectional scatter and space domain awareness. He has published three technical papers and is a member of SPIE.

Samuel D. Butler is a lieutenant colonel in the United States Air Force and an assistant professor at AFIT. He received his BS degree in applied physics with a computer science emphasis from

Brigham Young University, MS in applied physics and PhD from AFIT. His research interests include bidirectional scatter. He has advised seven MS and PhD students, and published 21 technical papers. He is a member of SPIE.

Michael A. Marciniak is a professor at AFIT. He received his BS degree in mathematics from St. Joseph's College, IN, BSEE from the University of Missouri-Columbia, and MSEE and PhD degrees from AFIT. His research interests include bidirectional scatter distribution and scatterometry of optical metasurfaces. He has advised 12 PhD dissertations and 55 MS theses, and published 42 refereed and 80 other technical papers. He is a senior member of SPIE.